Computer Physics Communications 193 (2015) 1–9

Contents lists available at ScienceDirect

Computer Physics Communications

journal homepage: www.elsevier.com/locate/cpc

A framework for stochastic simulations and visualization of biological electron-transfer dynamics

C. Masato Nakano [a,1], Hye Suk Byun [b,1], Heng Ma [c], Tao Wei [c,*], Mohamed Y. El-Naggar [b,d,e,*]

[a] Flintridge Preparatory School, La Canada Flintridge, CA 91011, USA
[b] Department of Physics & Astronomy, University of Southern California, Los Angeles, CA 90089-0484, USA
[c] Dan F. Smith Department of Chemical Engineering, Lamar University, Beaumont, TX 77710, USA
[d] Molecular and Computational Biology Section, Department of Biological Sciences, University of Southern California, Los Angeles, CA 90089, USA
[e] Department of Chemistry, University of Southern California, Los Angeles, CA 90089, USA

ARTICLE INFO

Article history:
Received 29 January 2015
Received in revised form
27 February 2015
Accepted 10 March 2015
Available online 31 March 2015

Keywords:
Visualization
Biological electron transfer
Molecular dynamics simulation
MM/PBSA
Kinetic Monte Carlo simulation

ABSTRACT

Electron transfer (ET) dictates a wide variety of energy-conversion processes in biological systems. Visualizing ET dynamics could provide key insight into understanding and possibly controlling these processes. We present a computational framework named VizBET to visualize biological ET dynamics, using an outer-membrane Mtr–Omc cytochrome complex in *Shewanella oneidensis* MR-1 as an example. Starting from X-ray crystal structures of the constituent cytochromes, molecular dynamics simulations are combined with homology modeling, protein docking, and binding free energy computations to sample the configuration of the complex as well as the change of the free energy associated with ET. This information, along with quantum-mechanical calculations of the electronic coupling, provides inputs to kinetic Monte Carlo (KMC) simulations of ET dynamics in a network of heme groups within the complex. Visualization of the KMC simulation results has been implemented as a plugin to the Visual Molecular Dynamics (VMD) software. VizBET has been used to reveal the nature of ET dynamics associated with novel nonequilibrium phase transitions in a candidate configuration of the Mtr–Omc complex due to electron–electron interactions.

© 2015 Elsevier B.V. All rights reserved.

1. Introduction

Reduction and oxidation reactions govern a variety of biological energy-conversion processes, including respiration. Electron transfer (ET) within and across biological molecules is the key process that essentially dictates these redox reactions [1]. Such biological ET reactions have been studied extensively in the past [2–5]. A remarkable example is the rapid ET from metal reducing bacteria such as *Shewanella oneidensis* MR-1 to extracellular metal oxides that serve as the terminal electron acceptors for anaerobic respiration [6–9]. Under certain conditions, *S. oneidensis* MR-1 produces electrically conductive bacterial nanowires that may mediate long-distance ET to extracellular oxidants [10–12]. A recent study has revealed that these *Shewanella* nanowires are membrane extensions decorated with the multiheme cytochromes MtrC and OmcA (Fig. 1(a)) [13]. These molecules had been previously identified as outer-membrane cytochromes and implicated as the terminal bacterial reductases of extracellular electron acceptors [14–17]. MtrC can associate with OmcA, in addition to forming a complex with the periplasmic decaheme cytochrome MtrA through transmembrane porin MtrB; this proposed arrangement has been described as the MtrCAB porin–cytochrome conduit, allowing ET across the cell envelope [17,18]. *Shewanella* can also express the MtrFDE conduit, which is homologous to MtrCAB, and MtrF (homolog of MtrC) has been shown to act as a terminal reductase in the absence of MtrC [19].

The localization of MtrC and OmcA along bacterial nanowires suggests that an outer-membrane lattice of cytochrome complexes may mediate ET over micrometer length scales, as schematized in Fig. 1(b) and (c) [13]. Here, each complex is comprised of two decaheme cytochromes, MtrC and OmcA, each of which contains 10 hemes (Fig. 1(b)). The iron (Fe) atom in each heme can exist in either of the two valence states, Fe^{2+} or Fe^{3+}. Conversion of the irons between Fe^{2+} and Fe^{3+} allows for the hopping of electrons between the hemes as shown in the inset of Fig. 1(b). Despite

* Corresponding authors.
E-mail addresses: twei@lamar.edu (T. Wei), mnaggar@usc.edu (M.Y. El-Naggar).
[1] These authors contributed equally to this work.

http://dx.doi.org/10.1016/j.cpc.2015.03.009
0010-4655/© 2015 Elsevier B.V. All rights reserved.

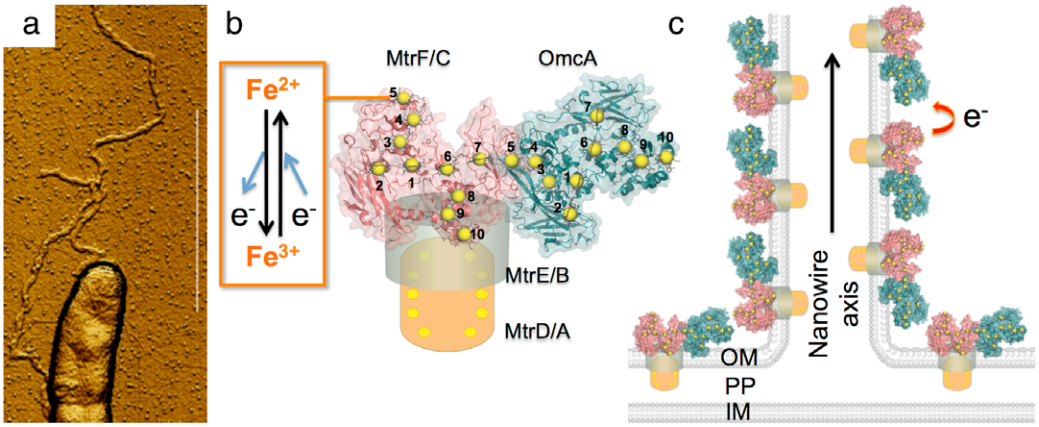

Fig. 1. (a) Atomic force microscope (AFM) image of a *Shewanella oneidensis* MR-1 cell and attached bacterial nanowires. The scale bar is 1 μm. (b) Structural model of an outer-membrane Mtr–Omc complex, where each yellow dot represents a heme group. Numerals show the numbering of the 10 hemes for both MtrC/F and OmcA. The inset shows that, in an oxidation reaction, ejection of an electron (e^-) converts the iron atom in a heme group from Fe^{2+} to Fe^{3+}, whereas, in a reduction reaction, injection of e^- converts it from Fe^{3+} to Fe^{2+}. (c) Hypothetical model of a bacterial nanowire, in which a lattice of Mtr–Omc complexes mediates long-distance electron transfer. The figure shows a central slice of the nanowire (IM: inner membrane, PP: periplasm, OM:outer membrane).

this plausible hypothesis, however, the microscopic nature of ET dynamics along these bacterial nanowires remains elusive.

Visualizing ET dynamics could provide key insight into understanding these fundamental processes and possibly controlling them for a wide range of applications including renewable energy and wastewater treatment [20]. Balabin et al. developed a plugin to the Visual Molecular Dynamics (VMD) software [21] that visualizes ET pathways in biomolecules based on a network model called Pathways [22]. Byun et al. [23] simulated the net electron flux through MtrF using, as input, the sequential heme-to-heme ET rates computed by Breuer et al. [24]. The latter were calculated from simulations of thermodynamic and electronic coupling parameters using molecular dynamics, fragment-orbital density functional theory (similar to divide-and-conquer density functional theory, DCDFT [25]), and the quantum mechanics/molecular mechanics (QM/MM) method [26,27]. The sequential heme-to-heme ET rates were recombined in kinetic Monte Carlo (KMC) simulations [28–31] to synthesize the global ET dynamics of MtrF [23]. These divide–conquer–recombine KMC (DCR-KMC) simulation results were visualized using VMD, but the visualization was limited to static snapshots.

To provide better insight into the dynamics of biological ET processes, we have developed a computational framework named VizBET. The framework consists of an entire workflow of the KMC simulation, and it animates the resulting ET dynamics using a new plugin to VMD. This paper presents key features and implementation details of VizBET, organized as follows. Section 2 describes the overall computational framework. Simulation and visualization results are presented in Section 3, and Section 4 contains a summary. In this work, we focus on demonstrating the visualization aspect of VizBET by using KMC simulation results with one possible protein–protein docking configuration. In future publications, we will present a more detailed procedure to screen for the most plausible docking complex structures, compute the binding free energy of these complexes with molecular mechanics/Poisson–Boltzmann surface area (MM/PBSA) [32–35], as well as intra/inter protein ET rates using QM/MM [26] simulations to parameterize the KMC simulation.

2. Methods

Fig. 2(a) summarizes the overall workflow of the VizBET framework, using an outer-membrane MtrF–OmcA cytochrome complex in *Shewanella oneidensis* MR-1 as an example (the crystal structure of MtrC is not yet available, so the homologous MtrF was used instead). The structures of the MtrF and OmcA molecules determined by X-ray diffraction are downloaded from the protein data bank (PDB) [36]. We first pre-process the PDB files to account for residues that were not resolved in the crystal structure with the aid of the homology-modeling Web server, I-TASSER [37]. The structural outputs from this pre-processing step are used as inputs to molecular-dynamics (MD) simulations that follow the trajectories of all atoms by numerically integrating Newton's equations of motion. Two MD simulations are performed for MtrF and OmcA molecules, respectively, in water. Individual MtrF and OmcA configurations taken from the MD simulations are used as inputs to a protein-docking program, ZDOCK [38], to predict the structure of the MtrF–OmcA complex. ZDOCK typically returns 2000 top configurations according to simple electrostatic and shape criteria. We have developed a C-RANK program to screen these configurations into a small subset of biologically plausible configurations, according to structural and ET criteria detailed below. Moreover, C-RANK serves as the starting point to further screen complex candidates by combining MD simulations, which re-solvate and relax the rigidly docked MtrF–OmcA complex structure, and the efficient binding free energy estimation with the method of MM/PBSA, which post-processes an ensemble of configurations from the MD trajectory with a combination of a force field and continuum solvent model [32–35]. The next step in VizBET is to perform DCR-KMC simulations for studying the ET dynamics in the selected MtrF–OmcA configurations. The DCR-KMC simulation component (Fig. 2(b)) within VizBET combines (1) either DCDFT or empirical approaches to compute the ET rates in a DC fashion, which are then used in (2) KMC simulations of global ET dynamics in the entire complex. We have also developed a plugin to the VMD software named ETViz to animate ET dynamics in the DCR-KMC simulations.

Currently, VizBET is implemented using the bash scripting language [39] to be used with the portable batch system (PBS) for job scheduling on a Linux cluster [40]. On high-end parallel supercomputers, we can alternatively use the Swift/T parallel scripting language for efficient distributed-memory workflow processing [41]. On a Grid of distributed parallel computers, the VizBET workflow can be converted to a directed acyclic graph to be executed using a scientific workflow management system such as Pegasus [42].

2.1. Structural modeling, MD simulations, docking and binding-free energy computations

The first step is to establish homology models for both proteins (MtrF and OmcA). We initially obtain X-ray structures of MtrF

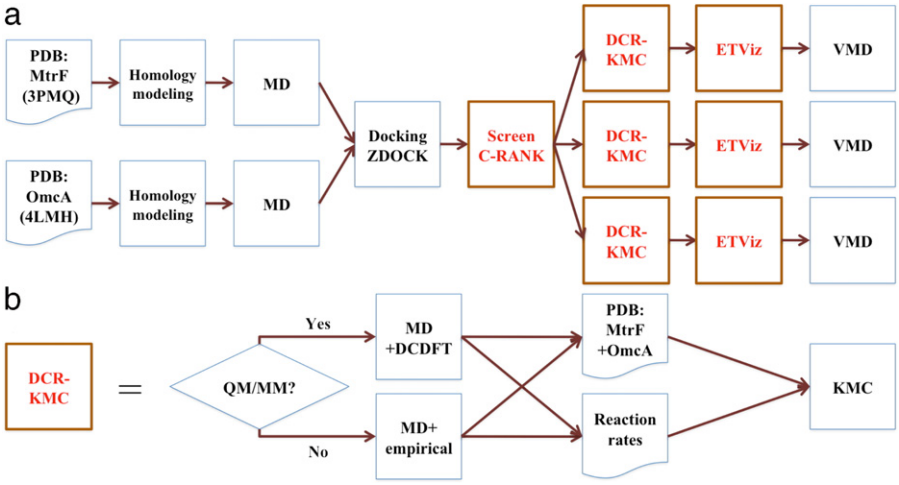

Fig. 2. (a) Workflow of the VizBET framework for biological ET visualization. Major new components developed for VizBET are represented by squares with thick lines. C-RANK consists of the further screening of ZDOCK results, re-solvation MD (molecular dynamics) and MM/PBSA (molecular mechanics/Poisson–Boltzmann surface area). (b) Detailed workflow of the DCR-KMC (divide–conquer–recombine kinetic Monte Carlo) simulation component. QM/MM: quantum mechanics/molecular mechanics; DCDFT: divide-and-conquer density functional theory.

and OmcA as determined from the PDB server [43]. The PDB codes for MtrF and OmcA are 3PMQ [44] and 4LMH [45], respectively. It should be noted that certain residues located near the N- and C-termini were not resolved in the crystal structures, likely due to the flexibility of those regions. The unresolved C-terminus residues from the X-ray studies were not included in our homology models, since they result from the purification tag of the recombinant protein. The signal peptide sequence preceding the cysteine residue of the N-terminal's LXXC cleavage and lipidation motif was also omitted from the homology model, since our goal is to study the mature proteins after cleavage and lipidation of the cysteine, which allows the anchoring of the lipoprotein to the membrane. As a result, our homology models target the amino-acid sequences of the membrane-bound forms of both proteins, starting with the cysteines, as listed in Appendix A. This leaves 25 and 16 N-terminus unresolved residues for MtrF and OmcA, respectively (italicized in Appendix A). In order to build a protein homology model by preserving the original crystal structure and the heme groups' positions while adding the missing residues, we adopt the following strategy. First, we predict the homology models of MtrF and OmcA by using the I-TASSER server [37] with each protein's sequence (Appendix A) and its original crystal structure as a reference. Here, the predicted homology models do not include heme groups and the coordinated calcium ions (Ca^{2+}). Second, the predicted structure of the homology model is superimposed on the original crystal structure so as to minimize the mean square displacement of all non-hydrogen atoms between the two structures using least-square fitting [46]. Third, the new residues from the optimal superposition are transferred and bonded onto the original crystal structure for each individual protein, in such a way that the heme groups and the coordinated Ca^{2+} ions are present in the original PDB files (one Ca^{2+} ion in 3PMQ; two Ca^{2+} ions in 4LMH) can be preserved at their original positions.

The second step is to establish both proteins' solvation structures. With the established homology models of the mature proteins, hydrogen atoms are explicitly added to both proteins. All of the amino acids are protonated (histidine (His) is treated neutral) with the exception of glutamic acid (Glu) and aspartic acid (Asp), which are taken as deprotonated. The N-terminus (NH_3^+) and the C-terminus (COO^-) are assigned with charges of $+e$ and $-e$ respectively. Those assignments result in a net charge of $-37e$ and $-31e$, respectively, for MtrF and OmcA including heme groups at pH 7. We perform MD simulations of individual MtrF and OmcA using the Gromacs software package (version 4.6.5) [47] and the Charmm 27 force-field parameters [48]. In both proteins, each Fe ion in a heme group is hexa-coordinated, i.e., two additional axial bonds are formed below and above the molecular plane of porphyrin macrocycle. We use the default harmonic bonding and dihedral potential in Charmm 27 for the Fe-N coordination bonding. In addition, to maintain the coordination geometry of Fe atom as the heme center, the angular potential of N–Fe–O (where O is the water oxygen) in Charmm 27 is adopted to represent the angular interaction of N–Fe–N and the equilibrium angle is set at 180 degree. The Ca^{2+} ions, which coordinate with proteins' amino residues, are included in the simulations and interact with proteins via van der Waals and electrostatic potentials. Initially, we relax the newly added residues by MD simulations in vacuum with a stepwise heating protocol from 60 K to 298.15 K. To remove the 'bad contacts' between the added residues and the rest, which lead to huge repulsion, only the added residues are relaxed while all the others are fixed at a low temperature. Subsequently, we obtain the solvated protein structure by MD simulations in an aqueous environment with the TIPS3P water model [48]. To neutralize the system, Na^+ counter ions are added in both vacuum and solvation simulations.

The third step is to obtain the predicted structure of the MtrF–OmcA complex using a protein-docking program, ZDOCK (version 3.0.2) [38]. As an input to the ZDOCK program, we use two PDB files for MtrF and OmcA, respectively, which are sampled from the MD simulations described above. ZDOCK predicts the structure of a protein–protein complex by treating each protein as a rigid body and docking them. The complex structures are scored using a combination of shape complementarity, electrostatics, and statistical potential terms. ZDOCK returns N top-ranked configurations according to the scoring as N PDB files labeled by the ranking (N is typically 2000).

As a fourth step, we use our C-RANK program to sub-select M biologically plausible complex candidates from the N ZDOCK outputs, where $M \ll N$, using two criteria: (1) the minimum inter-cytochrome heme–heme distance (edge-to-edge metric) should be less than 10 Å, to support rapid ET, and (2) the orientation of both proteins in the complex must be compatible with their lipophilic nature, allowing both N-terminus lipid binding sites to face a common plane that serves as proxy for the outer membrane.

In the ZDOCK rigid docking, the protein hydrogen atoms and the coordinated Ca^{2+} ions have been ignored. Those hydrogen atoms are finally re-added and Ca^{2+} ions are re-positioned at the original sites of both proteins according to their coordinated amino

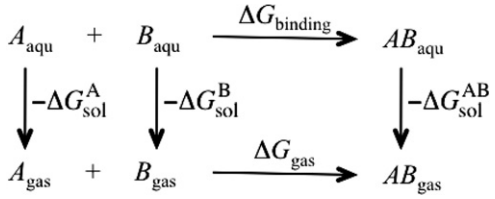

Fig. 3. Thermodynamic cycle to calculate the binding free energy of two proteins, A and B.

residues. Then the whole MtrF–OmcA complex is re-solvated with added counter ions following the stepwise heating protocol from 60 K to 298.18 K. After the heating, the complex is relaxed in the aqueous environment for 20 ns. The top candidates are now further screened by ranking the binding affinities based on the binding free energy calculated using the MM/PBSA method. For the MM/PBSA calculation, we have modified the recently developed suite of Bash/Perl scripts, GMXPBSA 2.1 [35], which combines the Gromacs software [47] and the Adaptive Poisson–Boltzmann Solver (APBS) program [49]. In MM/PBSA, the protein–protein binding free energy ($\Delta G_{binding}$) of A + B $\rightarrow$ AB is defined as the free energy difference between the complex (AB) and the sum of the free energies of the individual proteins (A and B) in aqueous environment as

$$\Delta G_{binding} = G^{AB}_{aqu} - G^{A}_{aqu} - G^{B}_{aqu}. \tag{1}$$

$\Delta G_{binding}$ is calculated with the thermodynamic cycle shown in Fig. 3 to include the complex solvation effect in the binding while minimizing the computational cost.

The corresponding binding free energy is expressed as

$$\Delta G_{binding} = \Delta G_{gas} - \Delta G^{A}_{sol} - \Delta G^{B}_{sol} + \Delta G^{AB}_{sol}. \tag{2}$$

$$\Delta G_{gas} = \left(\Delta\langle E_{intra}\rangle + \Delta\langle E_{LJ}\rangle + \Delta\langle E_{coul}\rangle\right) - T\langle\Delta S_{MM}\rangle. \tag{3}$$

$$\Delta G^{i}_{sol} = \Delta G^{i}_{polar} + \Delta G^{i}_{nonpolar}, \quad i = A,\ B\ or\ AB. \tag{4}$$

$$\Delta G^{i}_{nonpolar} = \gamma_i\langle SASA_i\rangle, \quad i = A,\ B\ or\ AB. \tag{5}$$

$$\Delta G_{polar} = \Delta G^{AB}_{polar} - \Delta G^{A}_{polar} - \Delta G^{B}_{polar}. \tag{6}$$

$$\Delta G_{nonpolar} = \Delta G^{AB}_{nonpolar} - \Delta G^{A}_{nonpolar} - \Delta G^{B}_{nonpolar}. \tag{7}$$

The symbol $\langle\,\rangle$ represents an average over configurations sampled from MD simulation. ΔG_{gas} in Eq. (3) is the binding free energy for the AB complex in the gas phase and consists of contributions from the averaged changes in intra-molecular interactions (E_{intra}), inter-molecular interactions that include Lennard-Jones (E_{LJ}) and Coulombic (E_{coul}) potentials, and the entropy contribution (S_{MM}), all computed with molecular mechanics. Due to its inaccuracy and debated contribution to the free energy, we follow the previous research [34,35,50] and ignore the entropy contribution. To reduce the computational time, we perform the MM/PBSA calculation with configurations from a single solvation MD simulation for the complex, rather than three separated solvation MD simulations for each individual component (A and B) and the complex. Accordingly, the change in the intra-molecular potential in the gas phase is ignored. The total solvation free energy (ΔG^{i}_{sol}) for component i (i = A, B, or AB) consists of both polar (ΔG^{i}_{polar}) and nonpolar ($\Delta G^{i}_{nonpolar}$) contributions (Eq. (4)). The dielectric constant (ε) inside proteins is set at 2.0. ΔG^{i}_{polar} is the protein–solvent electrostatic energy difference between the gas phase ($\varepsilon = 1$) and the solution phase ($\varepsilon = 80$), computed using the Poisson–Boltzmann method in a continuum implicit solvent medium and with grid spacing 0.5 Å. The nonpolar contribution ($\Delta G^{i}_{nonpolar}$) in Eq. (6) is estimated from the solvent accessible surface area (SASA) using the surface tension ($\gamma = 2.77$ kJ mol^{-1}nm^{-2}) [51]. A probe with the radius of 0.14 nm is used to identify the dielectric boundary in the SASA calculation. ΔG_{polar} and $\Delta G_{nonpolar}$ as shown in Eqs. (6) and (7) represent the itemized energy terms for the electrostatic and nonpolar potentials respectively between the complex and two individual proteins. In our MM/PBSA calculation, each component consists of a protein, 10 heme groups, and its coordinated calcium ion(s).

2.2. Divide–conquer–recombine kinetic Monte Carlo simulations of electron transfer

We perform KMC simulations [28–31] to study ET dynamics in the top-ranked MtrF–OmcA configurations selected. The KMC simulation [23] treats electron-hopping events in the MtrF–OmcA heme network with N_h (= 20) sites, where a heme site is labeled by index $i \in 1, \ldots, N_h$. The ith heme is either occupied by an electron ($n_i = 1$, corresponding to Fe^{2+}) or unoccupied ($n_i = 0$, corresponding to Fe^{3+}), where n_i is the electron occupation number of the ith heme. The system is characterized by electron hopping rates k_{ij} between a pair (i, j) of adjacent heme sites, electron injection rate α into selected entrance heme, and electron-ejection rate β from a selected exit heme. As implemented previously [23], we start the KMC simulation by emptying all sites and resetting the time to 0. At each KMC step, one of the following events occurs: (1) an electron is injected with rate α if the entrance heme is unoccupied; (2) an electron is ejected with rate β if the exit heme is occupied; or (3) an electron hops from heme i to one of its nearest-neighbor hemes j with rate k_{ij} if heme i is occupied and heme j is unoccupied. The probability of choosing a particular electron-hopping event is proportional to its specific hopping rate. This is implemented by choosing an event stochastically as follows: Let L be the total number of possible events and k_l ($l = 1, \ldots, L$) be the rate of the lth event; specific event l^* is chosen such that

$$\sum_{l=1}^{l*-1} k_l < \xi_1 k_{\text{total}} < \sum_{l=1}^{l*} k_l, \tag{8}$$

where ξ_1 is a random number uniformly distributed in the range (0, 1) and

$$k_{\text{total}} = \sum_{l=1}^{L} k_l \tag{9}$$

is the cumulative rate of all possible events. We displace the electron involved in the chosen event and increment the time by $\tau = -\ln(\xi_2)/k_{\text{total}}$, where ξ_2 is another random number. KMC steps are repeated for K ($\sim 10^6$) times to describe the time evolution of the system until the system reaches a steady state. The time-averaged electron occupation density at heme i is calculated as

$$\langle n_i\rangle = \frac{\sum_{t=1}^{K} n_i(t)\,\tau(t)}{\sum_{t=1}^{K}\tau(t)}, \tag{10}$$

where $\tau(t)$ is the time increment and $n_i(t)$ is the electron occupation number of the ith heme at the tth KMC step. The overall electron occupation density $\langle n\rangle$ is given by an average over all heme sites. The steady-state current J is obtained by dividing the net number of injected electrons during K KMC steps by the total elapsed time $\sum_{t=1}^{K}\tau(t)$.

VizBET supports two options in computing the ET rates k_{ij}. In both options, a thermodynamic integration protocol [52] is needed to estimate the change of the Gibbs free energy ΔG_{ij} and the reorganization energy λ associated with the ET from heme sites i to j [24,53,54]. The two options differ in the way the electronic

Table 1
Binding free energy computation from MM/PBSA.

$\Delta\langle E_{LJ}\rangle$ (kJ/mol)	$\Delta\langle E_{coul}\rangle$ (kJ/mol)	ΔG_{polar} (kJ/mol)	$\Delta G_{nonpolar}$ (kJ/mol)	$\Delta G_{binding}$ (kJ/mol)
-177.260 ± 8.412	18810.5 ± 12.203	-17945.519 ± 12.843	-21.237 ± 0.805	666.485 ± 17.835

coupling H_{ij} for the ET reaction is computed. In the first-principles QM/MM option [55,56], a divide–conquer–recombine (DCR) algorithmic framework [25] is employed. Here, the divide-and-conquer (DC) phase computes H_{ij} for each heme pair using the QM/MM method, where each QM calculation employs DC density functional theory (DFT). The calculated ET rates are used in the recombination phase to synthesize global ET dynamics using KMC simulations as described above. According to the non-adiabatic rate equation, the rate of ET, k_{ij}, from the ith heme to the jth heme is expressed as [1]

$$k_{ij} = \frac{2\pi}{\hbar}\langle|H_{ij}|^2\rangle \frac{1}{\sqrt{4\pi\lambda k_B T}} \exp\left(-\frac{\left(\Delta G_{ij}+\lambda\right)^2}{4\lambda k_B T}\right), \tag{11}$$

where T is the temperature, and $\hbar$ and k_B are the Planck and Boltzmann constants, respectively. To calculate inter-heme ET rates within a MtrF molecule, for example, Breuer et al. [24] estimated the electronic coupling by using the QM/MM method and a variant of DCDFT called fragment-orbital density functional theory.

The second option to calculate k_{ij} employs a phenomenological form of the non-adiabatic rate-equation [4],

$$k_{ij} = k_0 \exp\left(-\beta R_{ij} - \frac{\left(\Delta G_{ij}+\lambda\right)^2}{4\lambda k_B T}\right), \tag{12}$$

where R_{ij} is the edge-to-edge distance between hemes i and j, $k_0 = 10^{13}$ (s^{-1}), and β is a tunneling decay factor. Despite its simplicity, Eq. (12) correctly reflects the exponential decay of the tunneling probability and predicts ET rates in broad classes of biomolecules [4].

2.3. Visualization of electron transfer

To animate the ET dynamics in DCR-KMC simulations, we have developed a plugin [57] to the VMD software [21]. VMD is a molecular visualization program for large biomolecular systems using 3D graphics and built-in scripting. Our plugin is implemented using the Tcl scripting language [58]. We have used VMD version 1.9.1.

Multiple time frames from the KMC simulation are saved as a multi-frame PDB file, in which the n_i value of each Fe atom is written in the temperature-factor (BETA) field in its ATOM record. The Tcl script copies the PDB-BETA values to the USER fields in the TRAJECTORY data category in VMD, so that the time variation of the n_i values can be animated as color changes according to one of the built-in color scales in VMD. The animation can be shown in a display window or can be saved as a sequence of image files to create a movie file. The Fe atoms are represented by spheres with color-coded electron occupation n_i. The Fe charge dynamics are overlaid with the NewCartoon representation in VMD of the protein complex. This animation is used to examine the hopping of individual electrons within the heme network in the protein complex. Alternatively, VizBET can visualize the time averaged electron occupation,

$$\langle n_i\rangle_t = \frac{\sum_{s=1}^{t} n_i(s)\,\tau(s)}{\sum_{s=1}^{t}\tau(s)}. \tag{13}$$

In this way, we can animate how the time-averaged electron distribution converges to a steady state. Appendix B shows the Tcl script that reads a multi-frame PDB file named FeOcc.pdb and copies the BETA field of each atom into the USER field.

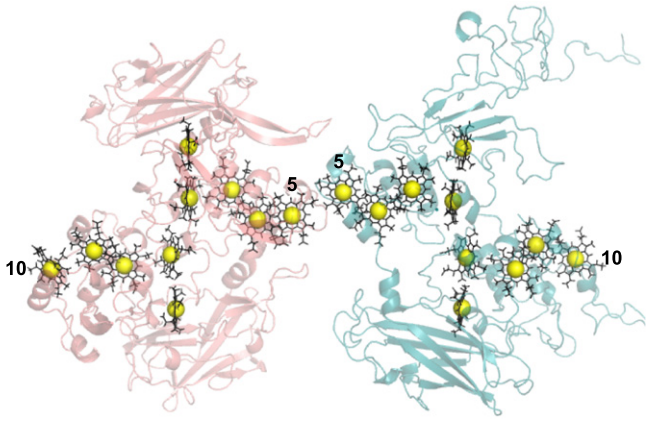

Fig. 4. The top-ranked MtrF–OmcA configuration according to our ET and orientation criteria, showing the 20-heme arrangement within the complex. Hemes 5 of both proteins define the inter-cytochrome contact with a 5.58 Å edge-to-edge distance.

3. Results

To illustrate the use of VizBET, we study lateral ET parallel to the outer membrane across the top ranked configuration of the MtrF–OmcA complex, according to the ET and orientation criteria described above, shown in Fig. 4. Remarkably, this MtrF–OmcA configuration is arranged similarly to the OmcA dimer crystallized by Edwards et al. [45], which is the only reported structure of two interacting decaheme cytochromes. This similarity further suggests that our screening procedure is capable of predicting biologically plausible structures of the complex. In this top ranked MtrF–OmcA configuration, heme 5 of each cytochrome serves as the site of cytochrome–cytochrome interaction, linking the two proteins' long axes from heme 10 of one to heme 10 of the other.

3.1. Binding free energy

For this example configuration (Fig. 4), MtrF–OmcA binding free energy is estimated with high throughput MM/PBSA computation by post-processing the configurations derived from the final 4.5 ns of MD simulation, at the stage of relaxing the complex in water after the rigid-docking. Table 1 lists the total binding free energy as well as the itemized energy terms. To be consistent with MD simulation, negligible salt concentration is used in MM/PBSA computation. In comparison, the polar contribution ($\Delta\langle E_{coul}\rangle$ and ΔG_{polar}) is dominant in the overall binding free energy. It should be noted that our interest here is to investigate the binding affinity, which is dependent on a particular relative orientation and position of both docking proteins. Consequently, there is no need to compute the exact docking free energy change, which includes the entropy contribution of the rotational motions of a ligand and a receptor. MM/PBSA can achieve high efficiency in computing the binding free energy without sampling orientational space in the docking, while still taking into account the thermal averaging and the important dehydration effect for two objects in contact in aqueous environment [59,60]. As shown in Table 1, the protein–solvent electrostatic potential, ΔG_{polar}, as a dominant term, is comparable with protein–protein electrostatic potential, $\Delta\langle E_{coul}\rangle$. Therefore, after the initial screening (based

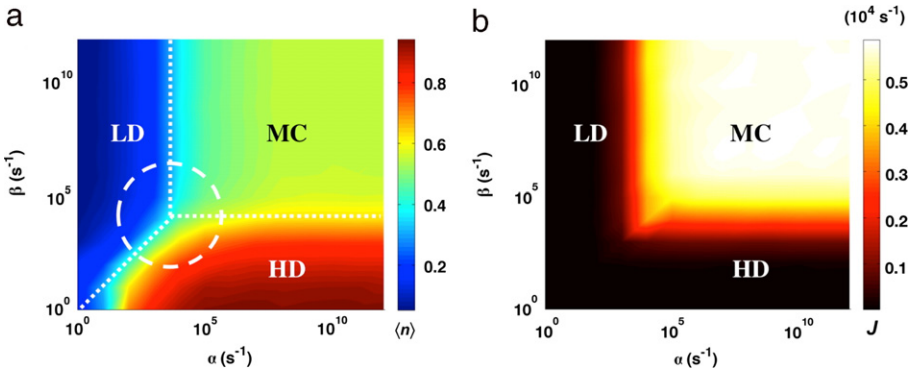

Fig. 5. (a) Phase diagram of the time-averaged electron occupation density $\langle n \rangle$ for all 20 hemes as a function of the incoming (α) and outgoing (β) ET rates. The white dotted lines delineate the low-density (LD), high-density (HD) and maximum current (MC) phases. The white dashed circle corresponds to experimentally estimated respiration rates. (b) The corresponding phase diagram of the net electron flux J.

on the criteria proteins' shape complementarity, neighboring heme groups' distance, and the proteins' lipid-site orientation), the orientation-dependent candidates can be further selected according to the binding free energy, which incorporates the dehydration effects. More detailed discussion about this screening will be provided in future work. The small fluctuations in these energy terms listed in Table 1 also demonstrate the structural stability of the complex and the convergence of the computation.

3.2. Nonequilibrium phase transitions

A multistep ET process has been hypothesized to allow long-distance electron transport through multiple complexes along a bacterial nanowire [13]. To examine this hypothesis along our top ranked configuration, the ET rates within the MtrF–OmcA complex are obtained by parameterizing and generalizing the H_{ij}, ΔG_{ij}, and λ calculated in Ref. [24] for MtrF. The H_{ij} parameters throughout the complex were fit to a single exponential $\langle |H_{ij}|^2 \rangle^{1/2}(r) = A \exp[-\beta(r - r_o)/2]$, where r is the edge-to-edge distance between i and j, $r_o = 3.6$ Å, $\beta = 1.65$ Å^{-1} and $A = 3.77$ meV, as presented in [24] for MtrF. Similarly, the ΔG_{ij}, and λ values computed for specific i–j pairs in MtrF are generalized throughout the whole combined MtrF–OmcA complex in our example.

Fig. 5 shows the KMC simulation results. Here, we chose the injection site as heme 10 in MtrF, and the ejection site as heme 10 in OmcA. By varying the incoming (α) and outgoing (β) ET rates, our simulation reveals a rich phase diagram for the MtrF–OmcA complex in the $\alpha - \beta$ plane (Fig. 5(a)). Three distinct phases are observed in the time-averaged occupation density of the icosaheme complex, similar to those recently reported for the decaheme MtrF [23]. A low-density (LD) phase, where the hemes are mostly oxidized, is observed when transport is limited by ET from intracellular donor molecules ($\alpha < \beta$). A high-density (HD) phase, where the hemes are mostly reduced, is observed when transport is limited by ET to extracellular electron acceptors ($\alpha > \beta$). Finally, a 'maximum-current' (MC) phase is observed when both α and β exceed the smallest heme-to-heme ET rate within the complex, which is $\sim 10^4$ s^{-1} along the octaheme path [24]. The high electron flux character of the MC phase, compared to the LD and HD phases, is easily identified in Fig. 5(b), which presents the phase behavior of the electron flux in the $\alpha - \beta$ plane. Intriguingly, cellular respiration measurements and estimates of the cellular cytochrome content translate to ET rates up to 10^3 s^{-1} per outer-membrane cytochrome [23]. This rate is located near the triple junction between the three phases; it appears that life operates where a small change in the electrochemical environment triggers large bioelectronic responses. It should be noted that these nonequilibrium phase transitions are a direct consequence of electron–electron interactions [61–63], which necessitate the use of many-body theory or simulations such as our KMC simulation.

3.3. Animation of electron-transfer dynamics

Fig. 6(a) shows a snapshot of the animation of the above KMC simulations, where $\alpha = 10^5$ s^{-1} and $\beta = 10^5$ s^{-1}. Such a static representation does not necessarily capture the nature of the many-electron ET dynamics, which is essential for understanding the microscopic mechanisms underlying the nonequilibrium phase transitions. The animation capability of VizBET is expected to bring about such dynamic insight. Three supplementary movie files, Movie S1–S3, located in Appendix C animate the ET dynamics corresponding to the LD ($\alpha = 10^2$ s^{-1} and $\beta = 10^5$ s^{-1}), HD ($\alpha = 10^5$ s^{-1} and $\beta = 10^2$ s^{-1}), and MC ($\alpha = 10^5$ s^{-1} and $\beta = 10^5$ s^{-1}) phases, respectively. Each movie depicts the final 500 KMC steps from a total of one million steps simulated. These movies show representative ET events in steady state for each phase after the initial transient vanishes. In the animation of the LD phase, a majority of the hemes are unoccupied, corresponding to the color blue. In the animation of the HD phase, a majority of the hemes are occupied, corresponding to the color red. Finally, in the MC phase, we observe extensive ET events, represented by more frequent and distributed color changes of the individual hemes. These movies help give insight into the possible roles and impact of individual hemes in the complex, for instance by identifying sites that act as carrier traps, or always reduced hemes which may act as electron donors to soluble acceptors capable of diffusing inside the complex [23].

To highlight ET events, we augment the above animations by representing each event as a directed edge. Namely, an ET event between two Fe atoms is represented by a cylinder that connects the participating Fe atoms. Here, one end of the cylinder attached to the source of ET is colored blue, while the other end connected to the destination of ET is colored red. Supplementary Movie S4 in Appendix C animates ET events in the MC phase ($\alpha = 10^5$ s^{-1} and $\beta = 10^5$ s^{-1}). Fig. 6(b) shows a snapshot of this animation.

As an alternative to the above movies, VizBET outputs the color-coded time-averaged electron occupation of each Fe atom as defined by Eq. (13). Fig. 6(c) shows such representation of the time-averaged occupation animation. This representation allows the user to see how the distribution of time-averaged occupation approaches a steady state distribution as time progresses. Supplementary Movie S5 in Appendix C animates time evolution of the time-averaged electron occupation in the MC phase ($\alpha = 10^5$ s^{-1} and $\beta = 10^5$ s^{-1}) for the initial 10,000 KMC steps.

4. Summary

We have described a computational framework named VizBET to visualize biological ET dynamics. This paper has presented VizBET using an outer-membrane MtrF–OmcA cytochrome complex

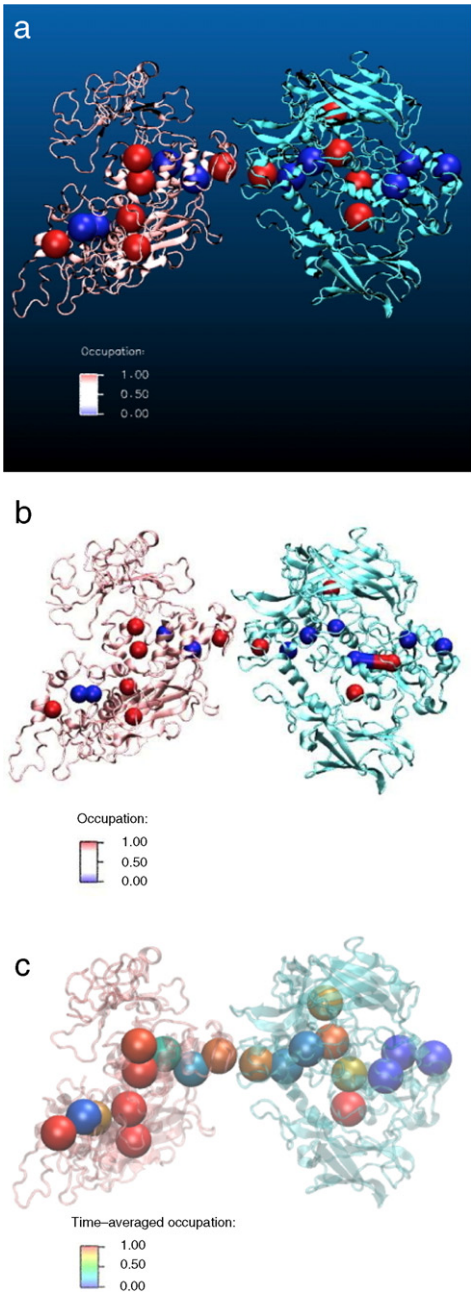

Fig. 6. Visualizing the KMC simulation of ET dynamics in the MtrF–OmcA complex. The Fe atoms are represented as spheres, and are overlaid with the NewCartoon representation of the entire protein complex, where MtrF and OmcA are represented in red and blue shades, respectively. Fe^{2+} and Fe^{3+} are represented by red and blue spheres, respectively. (a) A single snapshot from the final 500 KMC steps of the simulation. (b) A snapshot from the same simulation as (a), where an ET event is represented by a directed edge. (c) Time-averaged electron occupation, of each Fe atom (as defined by Eq. (13)). Injection/ejection parameters: $\alpha = \beta = 10^5\ s^{-1}$. (For interpretation of the references to color in this figure legend, the reader is referred to the web version of this article.)

in *Shewanella oneidensis* MR-1 as an example. Starting from X-ray structures of individual cytochromes, MD simulations are combined with homology modeling, protein docking, and binding free energy calculations to sample the configurations of the complex as well as the change of free energy associated with ET. Based on this information, combined with the QM calculation of electronic couplings, KMC simulations are performed to study global ET dynamics in the multiheme network of the complex. Visualization of the KMC simulation has been implemented as a plugin to the VMD software. Such spatiotemporal data visualizations and analyses [64] are expected to provide valuable insight into the microscopic mechanisms of ET processes in not only biological but also other novel nanostructures such as dislocation-mediated metallic nanowires in ceramics [65,66]. Currently, we are applying VizBET to a lattice of protein complexes and protein–solid interfaces. The visual simulation results will be published elsewhere.

Acknowledgments

The authors are grateful for insightful discussions with Dr. Liang Shi (Pacific Northwest National Lab) and Dr. Tom Clarke (University of East Anglia). HSB and MYE-N at the University of Southern California were supported by the U.S. Department of Energy, Office of Science, Office of Basic Energy Sciences, Division of Chemical Sciences, Geosciences, and Biosciences Grant DE-FG02-13ER16415. The work at Lamar University was supported by the Research Enhancement Grants (REG) fund from Lamar University, Oak Ridge National Laboratory (OLCF) Director Discretion Project and the National Science Foundation (NSF) Extreme Science and Engineering Discovery Environment (XSEDE) [67] program, which is supported by National Science Foundation grant number ACI-1053575. Simulations and visualization were performed at the USC Center for High Performance Computing, Oak Ridge National Laboratory and Texas Advanced Computing Center (TACC).

Appendix A

Sequences for building the MtrF and OmcA homology models in the FASTA format are provided below. The italicized residues were unresolved in the original crystal structures of MtrF (PDB file 3PMQ) and OmcA (PDB file 4LMH).

MtrF

*CGGSDGDDGSPGEPGKPPAMTISSL*NISVDKVAISDGIAQVDYQVSNQEN
QAVVGIPSATFIAAQLLPQGATGAGNSSEWQHFTSETCAASCPGTFVDH
KNGHYSYRFSATFNGMNGVTFLSDATQRLVIKIGGDALADGTVLPITNQ
HYDWQSSGNMLAYTRNLVSIDTCNSCHSNLAFHGGRYNQVETCVTCH
NSKKVSNAADIFPQMIHSKHLTGFPQSISNCQTCHADNPDLADRQNW
YRVPTMEACGACHTQINFPAGQGHPAQTDNSNCVACHNADWTANV
HSNAAQTSALAQFNASISSASMDANGTITVAVSLTNPTTGTAYADSADK
LKFISDLRIYANWGTSFDYSSRSARSIRLPESTPIAGSNGTYSYNISGLTVP
AGTESDRGGLAIQGRVCAKDSVLVDCSTELAEVLVIKSSHSYFNMSALT
TTGRREVISNAKCASCHGDQQLNIHGARNDLAGQCQLCHNPNMLADA
TATNPSMTSFDFKQLIHGLHSSQFAGFEDLNYPGNIGNCAQCHINDSTG
ISTVALPLNAAVQPLALNNGTFTSPIAAVCSNCHSSDATQNHMRQQGA
VFAGTKADATAGTETCAFCHGQGTVADVLKVHPIN

OmcA

*CGGSDGKDGEDGKPGV*VGVNINSTSTLKAKFTNATVDAGKVTVNFTLE
NANGVAVLGLTKDHDLRFGIAQLTPVKEKVGETEADRGYQWQAYINA
KKEPGTVPSGVDNLNPSTQFQANVESANKCDTCLVDHGDGSYSYTYQV
NVANVTEPVKVTYSADATQRATMELELPQLAANAHFDWQPSTGKTEG
IQTRNVVSIQACYTCHQPESLALHGGRRIDIENCASCHTATSGDPESGNS
IEFTYMIHAIHKGGERHTFDATGAQVPAPYKIIGYGGKVIDYGKVHYPQ
KPAADCAACHVEGAGAPANADLFKADLSNQACIGCHTEKPSAHHSSTD
CMACHNATKPYGGTGSAAKRHGDVMKAYNDSLGYKAKFSNIGIKNN
ALTFDVQILDNKDQPIGKEFISDPSAYTKSSIYFSWGIDKDYPAYTAGSR
YSDRGFALSNSKVSTYNEATKTFTIDSTNSNLKLPADLTGMNVELYAGV
ATCFNKGGYGVEDVVATPCSTDTRYAYIQDQPFRFKWNGTDTNSAAE
KRRAIIDTAKCSGCHNKEIVHYDNGVNCQACHTPDKGLKTDNTYPGTK
VPTSFAWKAHESEGHYLKYAGVQSGTVLKTDCATCHTADKSNVVTGIA
LGRSPERAWLYGDIKNNGAVIWVSSDAGACLSCHQKYLSDAAK
SHIETNGGILNGTSAADVQTRASESCATCHTPSQLMEAHGN

Appendix B

The following Tcl script is based on scripting examples provided at the Visual Molecular Dynamics (VMD) Web site, http://www.ks.uiuc.edu/Research/vmd/script_library/.

```
mol new FeOcc.pdb waitfor all
set all [atomselect top all]
set frame 0
set in [open FeOcc.pdb r]
set beta {}
while {[gets $ in line] !=-1 }{
    switch – [string range $ line 0 3] {
        END {
                $ all frame $ frame
                $ all set user $ beta
                set beta {}
                incr frame
        }
        HETA -
        ATOM {
                lappend beta [expr [string range $ line 60 65]]
        }
    }
}
```

Appendix C. Supplementary data

Supplementary Movies S1–S3 animate ET dynamics described in Section 3.3 for the low density, high density and maximum current phases, respectively. The corresponding electron injection (α) and ejection (β) rates are listed below. Movie S4 animates the same simulation as Movie S3, but with each ET event represented by a directed edge. In Movie S5, the time-averaged electron occupation is color-coded for the same simulation for the first 10,000 KMC simulation steps. Supplementary material related to this article can be found online at http://dx.doi.org/10.1016/j.cpc.2015.03.009.

References

[1] R.A. Marcus, N. Sutin, Electron transfers in chemistry and biology, Biochimica Biophys. Acta 811 (1985) 265–322.
[2] D.N. Beratan, J.N. Betts, J.N. Onuchic, Protein electron-transfer rates set by the bridging secondary and tertiary structure, Science 252 (1991) 1285–1288.
[3] C.C. Moser, J.M. Keske, K. Warncke, R.S. Farid, P.L. Dutton, Nature of biological electron-transfer, Nature 355 (1992) 796–802.
[4] H.B. Gray, J.R. Winkler, Electron tunneling through proteins, Q. Rev. Biophys. 36 (2003) 341–372.
[5] J.P. Lin, I.A. Balabin, D.N. Beratan, The nature of aqueous tunneling pathways between electron-transfer proteins, Science 310 (2005) 1311–1313.
[6] C.R. Myers, K.H. Nealson, Bacterial manganese reduction and growth with manganese oxide as the sole electron-acceptor, Science 240 (1988) 1319–1321.
[7] J.K. Fredrickson, M.F. Romine, A.S. Beliaev, J.M. Auchtung, M.E. Driscoll, T.S. Gardner, K.H. Nealson, A.L. Osterman, G. Pinchuk, J.L. Reed, D.A. Rodionov, J.L.M. Rodrigues, D.A. Saffarini, M.H. Serres, A.M. Spormann, I.B. Zhulin, J.M. Tiedje, Towards environmental systems biology of Shewanella, Nature Rev. Microbiol. 6 (2008) 592–603.
[8] M.Y. El-Naggar, S.E. Finkel, Live wires, Scientist 27 (2013) 38–43.
[9] M. Breuer, K.M. Rosso, J. Blumberger, J.N. Butt, Multi-haem cytochromes in Shewanella oneidensis MR-1: structures, functions and opportunities, J. Roy. Soc. Interface 12 (2015) 20141117.
[10] Y.A. Gorby, S. Yanina, J.S. McLean, K.M. Rosso, D. Moyles, A. Dohnalkova, T.J. Beveridge, I.S. Chang, B.H. Kim, K.S. Kim, D.E. Culley, S.B. Reed, M.F. Romine, D.A. Saffarini, E.A. Hill, L. Shi, D.A. Elias, D.W. Kennedy, G. Pinchuk, K. Watanabe, S. Ishii, B. Logan, K.H. Nealson, J.K. Fredrickson, Electrically conductive bacterial nanowires produced by Shewanella oneidensis strain MR-1 and other microorganisms, Proc. Natl. Acad. Sci. USA 103 (2006) 11358–11363.
[11] M.Y. El-Naggar, G. Wanger, K.M. Leung, T.D. Yuzvinsky, G. Southam, J. Yang, W.M. Lau, K.H. Nealson, Y.A. Gorby, Electrical transport along bacterial nanowires from Shewanella oneidensis MR-1, Proc. Natl. Acad. Sci. USA 107 (2010) 18127–18131.
[12] K.M. Leung, G. Wanger, M.Y. El-Naggar, Y. Gorby, G. Southam, W.M. Lau, J. Yang, Shewanella oneidensis MR-1 bacterial nanowires exhibit *p*-type, tunable electronic behavior, Nano Lett. 13 (2013) 2407–2411.
[13] S. Pirbadian, S.E. Barchinger, K.M. Leung, H.S. Byun, Y. Jangir, R.A. Bouhenni, S.B. Reed, M.F. Romine, D.A. Saffarini, L. Shi, Y.A. Gorby, J.H. Golbeck, M.Y. El-Naggar, Shewanella oneidensis MR-1 nanowires are outer membrane and periplasmic extensions of the extracellular electron transport components, Proc. Natl. Acad. Sci. USA 111 (2014) 12883–12888.
[14] C.R. Myers, J.M. Myers, Localization of cytochromes to the outer-membrane of anaerobically grown shewanella-putrefaciens Mr-1, J. Bacteriol. 174 (1992) 3429–3438.
[15] C.R. Myers, J.M. Myers, Cell surface exposure of the outer membrane cytochromes of Shewanella oneidensis MR-1, Lett. Appl. Microbiol. 37 (2003) 254–258.
[16] B.H. Lower, R. Yongsunthon, L. Shi, L. Wildling, H.J. Gruber, N.S. Wigginton, C.L. Reardon, G.E. Pinchuk, T.C. Droubay, J.F. Boily, S.K. Lower, Antibody recognition force microscopy shows that outer membrane cytochromes OmcA and MtrC are expressed on the exterior surface of shewanella oneidensis MR-1, Appl. Environ. Microbiol. 75 (2009) 2931–2935.
[17] D.J. Richardson, J.N. Butt, J.K. Fredrickson, J.M. Zachara, L. Shi, M.J. Edwards, G. White, N. Baiden, A.J. Gates, S.J. Marritt, T.A. Clarke, The porin-cytochrome' model for microbe-to-mineral electron transfer, Mol. Microbiol. 85 (2012) 201–212.
[18] L. Shi, B.W. Chen, Z.M. Wang, D.A. Elias, M.U. Mayer, Y.A. Gorby, S. Ni, B.H. Lower, D.W. Kennedy, D.S. Wunschel, H.M. Mottaz, M.J. Marshall, E.A. Hill, A.S. Beliaev, J.M. Zachara, J.K. Fredrickson, T.C. Squier, Isolation of a high-affinity functional protein complex between OmcA and MtrC: Two outer membrane decaheme c-type cytochromes of Shewanella oneidensis MR-1, J. Bacteriol. 188 (2006) 4705–4714.
[19] C. Bucking, F. Popp, S. Kerzenmacher, J. Gescher, Involvement and specificity of Shewanella oneidensis outer membrane cytochromes in the reduction of soluble and solid-phase terminal electron acceptors, FEMS Microbiol. Lett. 306 (2010) 144–151.
[20] B.E. Logan, Exoelectrogenic bacteria that power microbial fuel cells, Nature Rev. Microbiol. 7 (2009) 375–381.
[21] W. Humphrey, A. Dalke, K. Schulten, VMD: Visual molecular dynamics, J. Mol. Graph. 14 (1996) 33–38.
[22] I.A. Balabin, X.Q. Hu, D.N. Beratan, Exploring biological electron transfer pathway dynamics with the pathways plugin for VMD, J. Comput. Chem. 33 (2012) 906–910.
[23] H.S. Byun, S. Pirbadian, A. Nakano, L. Shi, M.Y. El-Naggar, Kinetic Monte Carlo simulations and molecular conductance measurements of the bacterial decaheme cytochrome MtrF, Chem. Electro. Chem. 1 (2014) 1932–1939.
[24] M. Breuer, K.M. Rosso, J. Blumberger, Electron flow in multiheme bacterial cytochromes is a balancing act between heme electronic interaction and redox potentials, Proc. Natl. Acad. Sci. USA 111 (2014) 611–616.
[25] F. Shimojo, R.K. Kalia, M. Kunaseth, A. Nakano, K. Nomura, S. Ohmura, K. Shimamura, P. Vashishta, A divide-conquer-recombine algorithmic paradigm for multiscale materials modeling, J. Chem. Phys. 140 (2014) 18A529.
[26] H. Lin, D.G. Truhlar, QM/MM: what have we learned, where are we, and where do we go from here? Theor. Chem. Acc. 117 (2007) 185–199.
[27] A.I. Krylov, P.M.W. Gill, Q-Chem: an engine for innovation, Wiley Interdiscip. Rev. Comput. Mol. Sci. 3 (2013) 317–326.
[28] A.B. Bortz, M.H. Kalos, J.L. Lebowitz, New algorithm for Monte-Carlo simulation of Ising spin systems, J. Comput. Phys. 17 (1975) 10–18.
[29] D.T. Gillespie, General method for numerically simulating stochastic time evolution of coupled chemical-reactions, J. Comput. Phys. 22 (1976) 403–434.
[30] K.A. Fichthorn, W.H. Weinberg, Theoretical foundations of dynamic Monte Carlo simulations, J. Chem. Phys. 95 (1991) 1090–1096.
[31] A.F. Voter, Introduction to the kinetic Monte Carlo metod, in: K.E. Sickafus, E.A. Kotomin, B.P. Uberuaga (Eds.), Radiation Effects in Solids, Springer, Dordrecht, The Netherlands, 2006.
[32] J. Srinivasan, T.E. Cheatham, P. Cieplak, P.A. Kollman, D.A. Case, Continuum solvent studies of the stability of DNA, RNA, and phosphoramidate — DNA helices, J. Am. Chem. Soc. 120 (1998) 9401–9409.
[33] I. Massova, P.A. Kollman, Computational alanine scanning to probe protein-protein interactions: A novel approach to evaluate binding free energies, J. Am. Chem. Soc. 121 (1999) 8133–8143.
[34] C. Paissoni, D. Spiliotopoulos, G. Musco, A. Spitaleri, GMXPBSA 2.0: A GROMACS tool to perform MM/PBSA and computational alanine scanning, Comput. Phys. Comm. 185 (2014) 2920–2929.
[35] C. Paissoni, D. Spiliotopoulos, G. Musco, A. Spitaleri, GMXPBSA 2.1: A GROMACS tool to perform MM/PBSA and computational alanine scanning, Comput. Phys. Comm. 186 (2015) 105–107.
[36] H.M. Berman, J. Westbrook, Z. Feng, G. Gilliland, T.N. Bhat, H. Weissig, I.N. Shindyalov, P.E. Bourne, The protein data bank, Nucl. Acids Res. 28 (2000) 235–242.
[37] A. Roy, A. Kucukural, Y. Zhang, I-TASSER: a unified platform for automated protein structure and function prediction, Nature Prot. 5 (2010) 725–738.
[38] B.G. Pierce, K. Wiehe, H. Hwang, B.H. Kim, T. Vreven, Z.P. Weng, ZDOCK server: interactive docking prediction of protein-protein complexes and symmetric multimers, Bioinformatics 30 (2014) 1771–1773.
[39] C. Newham, Learning the Bash Shell: Unix Shell Programming, O'Reilly Media, Sebastopol, CA, 2005.
[40] R.L. Henderson, Job scheduling under the Portable Batch System, Lecture Notes in Comput. Sci. 949 (1995) 279–294.

[41] J.M. Wozniak, T.G. Armstrong, M. Wilde, D.S. Katz, E. Lusk, I.T. Foster, Swift/T: Scalable data flow programming for many-task applications, ACM SIGPLAN Not. 48 (2013) 309–310.
[42] E. Deelman, J. Blythe, Y. Gil, C. Kesselman, G. Mehta, S. Patil, M.H. Su, K. Vahi, M. Livny, Pegasus: mapping scientific workflows onto the Grid, Grid Comput. 3165 (2004) 11–20.
[43] http://www.ncbi.nlm.nih.gov/.
[44] T.A. Clarke, M.J. Edwards, A.J. Gates, A. Hall, G.F. White, J. Bradley, C.L. Reardon, L. Shi, A.S. Beliaev, M.J. Marshall, Z.M. Wang, N.J. Watmough, J.K. Fredrickson, J.M. Zachara, J.N. Butt, D.J. Richardson, Structure of a bacterial cell surface decaheme electron conduit, Proc. Natl. Acad. Sci. USA 108 (2011) 9384–9389.
[45] M.J. Edwards, N.A. Baiden, A. Johs, S.J. Tomanicek, L.Y. Liang, L. Shi, J.K. Fredrickson, J.M. Zachara, A.J. Gates, J.N. Butt, D.J. Richardson, T.A. Clarke, The X-ray crystal structure of Shewanella oneidensis OmcA reveals new insight at the microbe-mineral interface, FEBS Lett. 588 (2014) 1886–1890.
[46] V.N. Maiorov, G.M. Crippen, Size-independent comparison of protein 3-dimensional structures, Proteins Struct. Funct. Genet. 22 (1995) 273–283.
[47] B. Hess, C. Kutzner, D. van der Spoel, E. Lindahl, GROMACS 4: algorithms for highly efficient, load-balanced, and scalable molecular simulation, J. Chem. Theory Comput. 4 (2008) 435–447.
[48] A.D. MacKerell, D. Bashford, M. Bellott, R.L. Dunbrack, J.D. Evanseck, M.J. Field, S. Fischer, J. Gao, H. Guo, S. Ha, D. Joseph-McCarthy, L. Kuchnir, K. Kuczera, F.T.K. Lau, C. Mattos, S. Michnick, T. Ngo, D.T. Nguyen, B. Prodhom, W.E. Reiher, B. Roux, M. Schlenkrich, J.C. Smith, R. Stote, J. Straub, M. Watanabe, J. Wiorkiewicz-Kuczera, D. Yin, M. Karplus, All-atom empirical potential for molecular modeling and dynamics studies of proteins, J. Phys. Chem. B 102 (1998) 3586–3616.
[49] N.A. Baker, D. Sept, S. Joseph, M.J. Holst, J.A. McCammon, Electrostatics of nanosystems: Application to microtubules and the ribosome, Proc. Natl. Acad. Sci. USA 98 (2001) 10037–10041.
[50] T.J. Hou, J.M. Wang, Y.Y. Li, W. Wang, Assessing the performance of the MM/PBSA and MM/GBSA Methods. 1. the accuracy of binding free energy calculations based on molecular dynamics simulations, J. Chem. Inf. Model. 51 (2011) 69–82.
[51] S.P. Brown, S.W. Muchmore, Large-scale application of high-throughput molecular mechanics with Poisson–Boltzmann surface area for routine physics-based scoring of protein-ligand complexes, J. Med. Chem. 52 (2009) 3159–3165.
[52] V.A. Ngo, Parallel-pulling protocol for free-energy evaluation, Phys. Rev. E 85 (2012) 036702.
[53] M. Breuer, P. Zarzycki, J. Blumberger, K.M. Rosso, Thermodynamics of electron flow in the bacterial deca-heme cytochrome MtrF, J. Am. Chem. Soc. 134 (2012) 9868–9871.
[54] M. Breuer, P. Zarzycki, L. Shi, T.A. Clarke, M.J. Edwards, J.N. Butt, D.J. Richardson, J.K. Fredrickson, J.M. Zachara, J. Blumberger, K.M. Rosso, Molecular structure and free energy landscape for electron transport in the decahaem cytochrome MtrF, Biochem. Soc. Trans. 40 (2012) 1198–1203.
[55] A. Warshel, M. Karplus, Calculation of ground and excited-state potential surfaces of conjugated molecules. 1. formulation and parametrization, J. Am. Chem. Soc. 94 (1972) 5612–5625.
[56] A. Warshel, M. Levitt, Theoretical studies of enzymic reactions — dielectric, electrostatic and steric stabilization of carbonium–ion in reaction of lysozyme, J. Mol. Biol. 103 (1976) 227–249.
[57] http://www.ks.uiuc.edu/Research/vmd/script_library/.
[58] J.K. Ousterhout, K. Jones, Tcl and the Tk Toolkit, second ed., Addison-Wesley, Boston, MA, 2009.
[59] T. Wei, M.A. Carignano, I. Szleifer, Lysozyme adsorption on polyethylene surfaces: why are long simulations needed? Langmuir 27 (2011) 12074–12081.
[60] T. Wei, M.A. Carignano, I. Szleifer, Molecular dynamics simulation of lysozyme adsorption/desorption on hydrophobic surfaces, J. Phys. Chem. B 116 (2012) 10189–10194.
[61] I. Neri, N. Kern, A. Parmeggiani, Totally asymmetric simple exclusion process on networks, Phys. Rev. Lett. 107 (2011) 068702.
[62] T. Chou, K. Mallick, R.K.P. Zia, Non-equilibrium statistical mechanics: from a paradigmatic model to biological transport, Rep. Progr. Phys. 74 (2011) 116601.
[63] M. Gorissen, A. Lazarescu, K. Mallick, C. Vanderzande, Exact current statistics of the asymmetric simple exclusion process with open boundaries, Phys. Rev. Lett. 109 (2012) 170601.
[64] D. Bhattarai, B.B. Karki, Atomistic visualization: Space–time multiresolution integration of data analysis and rendering, J. Mol. Graph. 27 (2009) 951–968.
[65] A. Nakamura, K. Matsunaga, J. Tohma, T. Yamamoto, Y. Ikuhara, Conducting nanowires in insulating ceramics, Nature Mater. 2 (2003) 453–456.
[66] K. Tsuruta, E. Tochigi, Y. Kezuka, K. Takata, N. Shibata, A. Nakamura, Y. Ikuhara, Core structure and dissociation energetics of basal edge dislocation in alpha-Al_2O_3: a combined atomistic simulation and transmission electron microscopy analysis, Acta Mater. 65 (2014) 76–84.
[67] J. Towns, T. Cockerill, M. Dahan, I. Foster, K. Gaither, A. Grimshaw, V. Hazlewood, S. Lathrop, D. Lifka, G.D. Peterson, R. Roskies, J.R. Scott, N. Wilkins-Diehr, XSEDE: Accelerating scientific discovery, Comput. Sci. Eng. 16 (2014) 62–74.